



# Development of covalent-organic frameworks derived hierarchical porous hollow carbon spheres based LiOH composites for thermochemical heat storage

Xiangyu Yang<sup>a,b</sup>, Shijie Li<sup>a,\*</sup>, Jianguo Zhao<sup>a,b,\*</sup>, Hongyu Huang<sup>c</sup>, Lisheng Deng<sup>d</sup>

<sup>a</sup> Institute of Carbon Materials Science, Shanxi Datong University, Datong 037009, Shanxi, China

<sup>b</sup> School of Materials Science and Engineering, Taiyuan University of Technology, Taiyuan 030024, Shanxi, China

<sup>c</sup> Key Laboratory of Renewable Energy, Guangdong Provincial Key Laboratory of New and Renewable Energy Research and Development, Guangzhou Institute of Energy Conversion, Chinese Academy of Sciences, Guangzhou 510640, Guangdong, China

<sup>d</sup> Guangdong Intelligent Filling Technology Limited Company, Foshan 528137, Guangdong, China

## ARTICLE INFO

### Article history:

Received 7 May 2022

Revised 13 June 2022

Accepted 14 June 2022

Available online 18 June 2022

### Keywords:

Activated hollow spherical carbon  
Hierarchical porous architectures  
LiOH-THS composite material  
Storage ability  
COFs-derived carbonaceous materials

## ABSTRACT

Under the joint assistance of its excellent storage strength, accessible long storage lifespan, and high heat utilization efficiency, salt hydrate-based thermochemical heat storage (THS) materials give renewable energy an important outlet to alleviate the pressure of underutilization. Herein, an activated hollow spherical carbon (AHSC) with hierarchical porous architectures converted from covalent-organic frameworks (COFs) is constructed and utilized as the supporting matrix for LiOH-THS composite material for the first time. The obtained Li/AHSC3 composites have distinguished hydration performance while manifesting impressive storage ability up to 1916.4 kJ kg<sup>-1</sup> with low operating temperature stemming from the collective effect of the void spherical framework, multimodal porosity, and high surface area of AHSC3. And the Li/AHSC3-40 composite with evidently progressed thermal conductivity is capable of realizing 94.5% heat preservation after twenty-five adsorption-desorption cycles, exhibiting its eminent cyclability and great heat transfer performance. This study not only brings new hope for overcoming the underutilization of low-grade heat but also may enlighten new ideas for enriching the application scenarios of COFs-derived carbonaceous materials.

© 2022 Science Press and Dalian Institute of Chemical Physics, Chinese Academy of Sciences. Published by ELSEVIER B.V. and Science Press. All rights reserved.

## 1. Introduction

Energy is the driving force and lifeline of national economic development, and the rational exploitation and efficient utilization of energy are the sources of civilization and social progress [1,2]. Under the continuous acceleration of global fossil energy consumption, the subsequent pollution problems have become increasingly prominent, and mankind is already encountering a severe double crisis of energy and the environment [3,4]. In the face of the harsh reality, countries around the world have not only gradually turned their attention to the exploitation as well as utilization of green and clean energy (solar energy, hydrogen energy, tidal energy, wind energy, etc.) as well as the improvement of the efficiency of traditional energy, but also strived to achieve the global energy revolution and the goal of “carbon peak and carbon

neutrality” by working together on the two measures [5,6]. Nevertheless, the promotion and utilization of renewable energy with broad application prospects are affected by factors such as intermittent and uneven geographical distribution, and the mismatch between the energy supply and consumption makes it inefficient and difficult to be directly utilized [7]. On the other hand, the underutilization of a substantial amount of industrial waste heat also stands on the opposite side of the low-carbon and sustainable development of new energy strategies [8]. Therefore, the exploitation of efficient and sustainable energy conversion as well as storage technology is a critical part of the new energy strategy [9]. It can not only balance the contradiction of uneven energy supply and demand by storing and supplying energy on demand but also be able to match different energy needs to promote its application in different fields [10].

By virtue of its tailorable 2D or 3D topological geometries and porosity, tailorable chemical and structural selectivity owing to the functionalization of organic building blocks as well as high surface area, covalent organic frameworks (COFs) have been applied in

\* Corresponding authors.

E-mail addresses: [li841974@sina.com](mailto:li841974@sina.com) (S. Li), [zhaojianguo@sxtdx.edu.cn](mailto:zhaojianguo@sxtdx.edu.cn) (J. Zhao).

the areas of energy, environment, as well as photocatalysis implementations [11,12]. Nevertheless, restricted by their pure organic structure, most COFs face the inherent flaw of unsatisfactory thermal conductivity, which greatly narrows their application prospects [13,14]. As a countermeasure, the strategy of converting COF into carbonaceous materials has been proposed and the synthesized carbon materials have shown outstanding performance in many fields thanks to the integration of the diverse structural topology and abundant pores of COF precursors and the eminent thermal conductivity of carbon materials [15,16]. Despite the porous carbon materials with COF as the precursor showing significant advantages over traditional carbon materials, the carbonaceous materials directly carbonized from COF mostly involve the monotonic porosity and irregular geometric configurations, which creates an indelible obstacle to the efficient diffusion and mass transfer of molecules [17,18]. In response, hollow carbon derived from COFs with huge cavities and hierarchical porous structures emerged and occupied a pivotal position of practical implementation in various fields owing to their high surface-volume ratios as well as diffusion favorable open architecture [19,20]. Unfortunately, the expansion of the porosity framework in the hollow carbon will inevitably produce back phagocytosis against the surface area, which counteracts the full contact of the reactant with the supporting matrix [21]. Under such a circumstance, it is urgently needed to fabricate hollow carbonaceous materials with high surface area through carefully regulating the monomer and optimizing the structure to achieve the goal of highlighting the superiority of the two structures while avoiding their respective defects. Furthermore, it should be pointed out that in sharp contrast to its extensive implementation in other territories, carbonaceous materials derived from COFs are invisible in the area of heat storage with broad engineering implementation prospects.

Heat storage systems, which not only can solve the dilemma of intermittent time, spatial dispersion, and intensity instability in the conversion and utilization of different forms of energy, but also achieve technical and economic macro application, have provided important technical support for the transformation of the energy structure, and it has also been widely implemented in the areas of renewable energy applications, industrial waste heat utilization, building energy applications, as depicted in Fig. 1 [22–24]. Under

the joint assistance of its high energy density, long storage lifespan, wide operating temperature range as well as high comprehensive heat utilization efficiency, thermochemical heat storage (THS) systems have demonstrated more impressive performance than sensible and latent heat storage systems in practical applications such as enhancing the flexibility of power systems and the efficiency of photothermal conversion [25–27]. Relying on the non-toxic and easy availability of its initiators and the direct reaction mechanism without side reactions, hygroscopic salt THS materials have become one of the most widely applied THS systems [28–30]. Furthermore, the actual temperature (<200 °C) of low-grade heat sources (industrial waste heat resources, solar thermal energy) has a large intersection with the operating temperature range of many salt hydrate THS materials (70–150 °C) [31,32]. In the face of this reality, the emergence of LiOH with relatively low operating temperature has brought new possibilities between salt hydrate heat storage materials and the use of low-grade heat sources [33,34]. Regrettably, defects such as deliquescent and crusts, unsatisfactory cycling performance, and poor thermal conductivity that hinder the implementation of salt hydrates can still be seen in pure LiOH, which not only severely narrows its promotion and application scope, but also makes the vision of realizing the use of low-grade energy by salt hydrate THS material an unreachable mirage [35,36]. Hence, reasonable design and construction of a LiOH·THS material with extraordinary storage strength and hydration properties, as well as prominent cyclability and heat transfer performance with the help of a porous supporting matrix to realize effective utilization of low-temperature heat energy remain a thorny task.

In this work, we report the construction of an activated hollow spherical carbon (AHSC) with hierarchical porous architectures converted from COFs and its implementation as the supporting matrix for LiOH·THS composites. To the best of our knowledge, compared with its extensive research in different territories, the implementation of COFs-derived porous carbonaceous materials in thermochemical heat storage has not been reported so far. The fabricated Li/AHSC3 THS composite material not only has prominent storage ability and hydration property but also exhibits distinguished thermal conductivity and cyclability, which verifies the indispensability of AHSC3 as a supporting matrix in enhancing

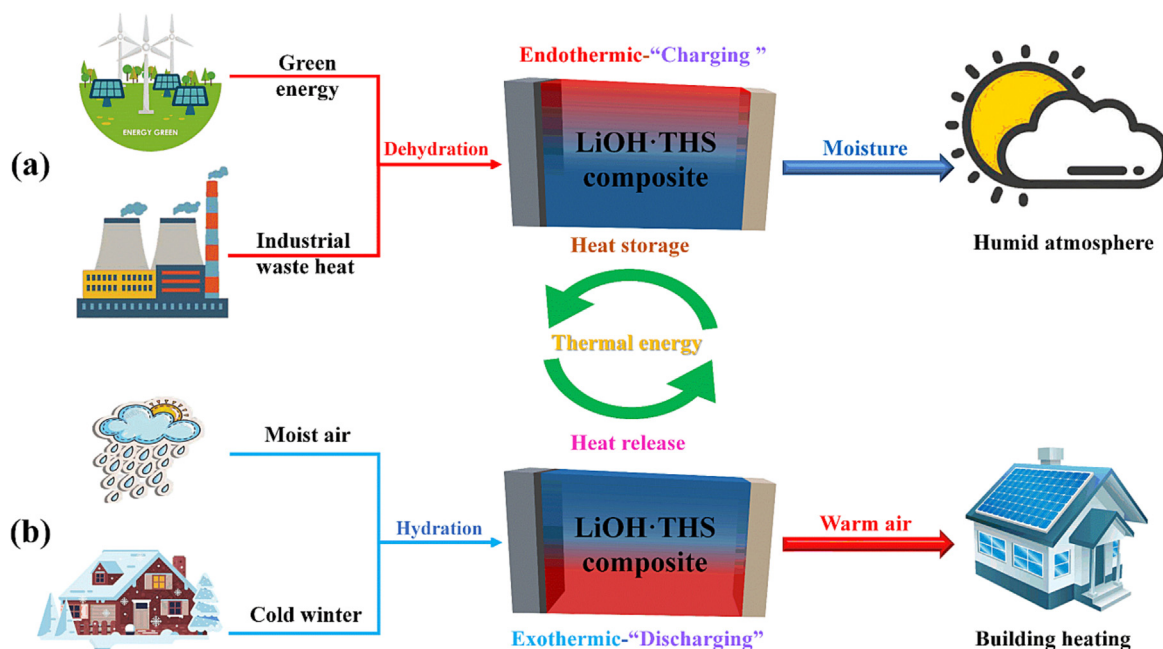


Fig. 1. Diagrammatic sketch of the LiOH·THS composite for low-grade heat energy storage and residential implementation (a) heat storage process, (b) heat release process.

the storage strength of the composite materials and its unlimited future in the conversion and implementation of renewable energy.

## 2. Experimental

### 2.1. Preparation of hollow covalent-organic framework (Hollow COF)

Typically, 1,3,5-tris(4-aminophenyl)-benzene (50 mg) and 4-formylphenylboronic acid (75 mg) were dissolved in a mixed solvent of 1,4-dioxane/mesitylene (1/1 v/v, 5 mL) and added into a 50 mL Schlenk tube. The mixture was sonicated for 5 min and degassed through three freeze–pump–thaw cycles. The reaction mixture was reacted at 120 °C for 72 h. After the reaction was completed, the precipitate was isolated by filtration and washed with anhydrous 1,4-dioxane several times, and the obtained crude product was purified by Soxhlet extraction using tetrahydrofuran. Finally, light yellow hollow COF powder was obtained after drying at 60 °C under vacuum for 12 h.

### 2.2. Preparation of hollow COF derived hollow spherical carbon (CHSC) and AHSC

In a typical carbonization process, the hollow COF powder was heated to 700, 800, and 900 °C at a ramp rate of 5 °C min<sup>−1</sup> and kept for 2 h under Ar atmosphere. After cooling to room temperature, the resulting black powder was treated with water at 70 °C for 10 h. Finally, CHSC was obtained after the crude product was washed with deionized water and methanol and then dry at 80 °C under vacuum for 10 h, denoted as CHSC(700), CHSC(800), and CHSC(900), respectively.

AHSC was prepared by potassium hydroxide (KOH) activation. Typically, CHSC(800) (0.3 g) was mixed with a 10 mL aqueous solution containing 0.9 g KOH and stirred for 2 h. After drying at 100 °C, the resulting mixture was heated to 800 °C at a ramp rate of 5 °C min<sup>−1</sup> and kept for 1 h under Ar atmosphere. After cooling to room temperature, the resulting black powder was washed with HCl (1 M) for 4 h and then washed with deionized water until pH = 7. Finally, the activated hollow spherical carbon was obtained after drying at 80 °C under vacuum for 10 h, denoted as AHSC3. The preparation route of hollow COF, CHSC(800), and AHSC3 is depicted in Fig. 2. In addition, AHSC2 and AHSC4 were synthesized by the same method, except that the mass ratio of CHSC(800) to KOH was changed to 1:2 and 1:4, respectively.

### 2.3. Preparation of LiOH thermochemical heat storage composites

In a typical preparation procedure, the AHSC3 powder (50 mg) was added to 25 mL of deionized water with different LiOH ratios and stirred at room temperature for 2 h. Next, the solution was transferred into a 50 mL Teflon-lined stainless steel autoclave and kept in an oven at 160 °C for 15 h. After the autoclave was cooled to room temperature, the resulting solution was dried at 200 °C for 2 h to obtain a completely dehydrated target LiOH-THS composite. The target products with different LiOH ratios (20 wt %, 30 wt %, 40 wt %, 50 wt %) were denoted as Li/AHSC3-20, Li/AHSC3-30, Li/AHSC3-40 and Li/AHSC3-50, respectively. For comparison, Li/CHSC(700)-20, Li/CHSC(800)-20, Li/CHSC(900)-20, Li/AHSC2-20 and Li/AHSC4-20 were synthesized the same method, except that the supporting matrix was changed to CHSC(700), CHSC(800), CHSC(900), AHSC2 and AHSC4, respectively. The reagents and characterization are shown in the [Supplementary Material](#).

## 3. Results and discussion

### 3.1. Morphological features and chemical structure

The morphological and microstructural features of hollow COF, CHSCs, and AHSCs were carefully studied through SEM and TEM analyses. As depicted in Fig. 3(a), the as-synthesized COF spliced by many intertwined nanoplates exhibits a unique 3D spherical shape and its interior cavity architecture is also unambiguously confirmed by broken nanospheres. For the purpose of getting a clear insight into the morphological evolution and formation mechanism of the hollow structure of the fabricated COF, time-dependent experiments were carried out. As displayed in Fig. S1 (a), the nanosheets assembled into solid spherical-like nanoparticles after the reaction was carried out for 3 h. After continuing the reaction for 9 h, the solid microspheres were formed (Fig. S1b). When the reaction was carried out for 18 h (Fig. S1c), tiny cavities were formed in the solid microspheres due to the dissolution of the crystallites from the inner core and migration out of the spheres, which is also known as the inside-out Ostwald-ripening process [37,38]. Finally, hollow microspheres with a well-defined hierarchical structure were obtained after 72 h of reaction (Fig. S1d).

After pyrolysis, the obtained CHSC(800) (Fig. 3b) maintains the spherical shape of the hollow COF with nanosheet structure, and its corresponding hollow architecture is also inherited intact. After undergoing severe chemical activation, both AHSC2 (Fig. S2a) and

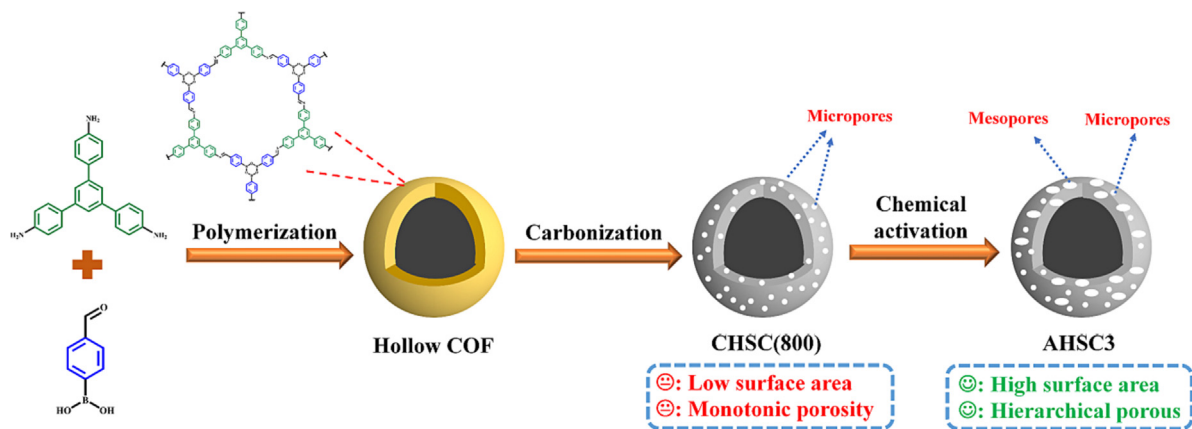
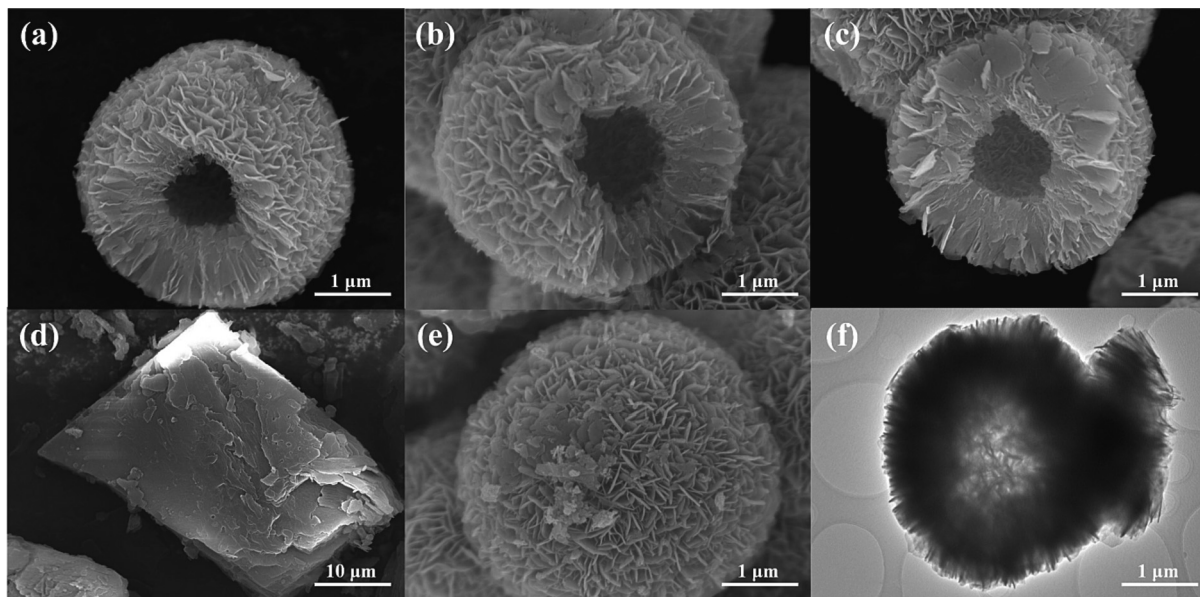


Fig. 2. Synthetic routes of hollow COF, CHSC(800), and AHSC3.





**Fig. 3.** SEM images of (a) Hollow COF, (b) CHSC(800), (c) AHSC3, (d) LiOH, (e) Li/AHSC3-40 and TEM image of (f) AHSC3.

AHSC3 (Fig. 3c) well maintain the external morphology and spherical geometry of CHSC(800). Meanwhile, Fig. 3(f) presents that the void framework, as well as the structural integrity of the precursor, are also not compromised. It is noteworthy that when the amount of the activator is changed to 1:4, AHSC4 (Fig. S2b) is unable to maintain the topographical features of CHSC(800) but collapses internally and agglomerates into clumps with irregular shapes as a result of the overly extravagant activation process caused by high activator dosage. The loss of the geometric integrity of AHSC4 caused by this aggressive activation not only deprives its precursor of the precious structural privileges but may also backfire on its potential as a supporting matrix [39]. Besides, Fig. 3(d) elucidates the exaggerated size and conspicuous aggregation of lithium hydroxide before it is composited with the supporting matrix, which not only lays a hidden danger for its reaction with the vapor but also the root source of the severe attenuation of its storage strength, the undesired cyclability and the difficulty of its engineering application. Interestingly, Fig. 3(e) displays that the hygroscopic salt grains are homogeneously dispersed among the hierarchically interconnected nanoplates of the supporting matrix in Li/AHSC3-40, which greatly suppresses the crusting and agglomeration of salt grains while also contributing to the enhancement of the hydration properties of hygroscopic salts.

The chemical composition and structure of hollow COF, CHSC, and AHSC were resolved by FT-IR and XRD. Fig. S4 shows that in comparison with 1,3,5-tris(4-aminophenyl)-benzene and 4-formylphenylboronic acid, no absorption peaks belonging to the N–H ( $3435$  and  $3352$   $\text{cm}^{-1}$ ) and C=O ( $1673$   $\text{cm}^{-1}$ ) are observed in the hollow COF. In contrast, absorption peaks assign to the C=N ( $1612$   $\text{cm}^{-1}$ ) and B–O ( $689$   $\text{cm}^{-1}$ ) are found in the hollow COF, indicating the occurrence of the amine-aldehyde condensation reaction and the successful preparation of the hollow COF [40]. And the diffraction peaks of the XRD pattern (Fig. S5) of the COF are consistent with those reported previously, providing further evidence for its successful preparation [41]. Furthermore, the TGA curve (Fig. S6) indicates that the hollow COF only exhibits significant weight loss between  $350$ – $600$   $^{\circ}\text{C}$  owing to the decomposition of functional groups throughout the pyrolysis process, which results in  $700$ ,  $800$ , and  $900$   $^{\circ}\text{C}$  being identified as carbonization temperatures. As depicted in Fig. 4(a), the distinct peaks of hollow COF all disappear after pyrolysis, while broad peaks

corresponding to the (002) and (101) of amorphous carbon respectively appear near  $24^{\circ}$  and  $44^{\circ}$ , indicating that hollow COF has been pyrolyzed into carbonaceous materials. Noticeably, the peak intensities near  $24^{\circ}$  of all the resulting AHSCs after chemical activation are conspicuously weakened and broadened compared with the directly carbonized CHSCs, indicating an improvement in the defectivity and porosity of the AHSCs [42]. To further examine the structural evolution before and after activation of the supporting matrix from a quantitative perspective, Raman spectroscopy was performed on a series of CHSCs and AHSCs. As depicted in Fig. 4(b), all supporting matrices display two distinct peaks at  $1337$   $\text{cm}^{-1}$  (D band) and  $1586$   $\text{cm}^{-1}$  (G band), representing disordered carbon and graphitized carbon, respectively. And the intensity ratio of the two peaks ( $I_D/I_G$ ) is able to assess the defectivity of the carbonaceous materials [43]. On the one hand, the  $I_D/I_G$  ratios of CHSC(700) (0.88), CHSC(800) (0.93), and CHSC(900) (0.94) show an upward trend in synchronization with the carbonization temperature, indicating the pyrolysis temperature has a positive effect on the improvement of defectivity in the supporting matrix and the increase in defects could create more microscopic diffusion channels that are conducive to vapor diffusion and mass transfer. On the other hand, the  $I_D/I_G$  ratios of all AHSCs are higher than that of CHSCs and the rising level is proportional to the activation ratio, confirming the practicality and effectiveness of KOH activation in expanding the pore pattern of the carbonaceous supporting matrix. As depicted in Fig. 4(c), all Li/AHSC3 materials display the diffraction peaks of lithium hydroxide, while the peak of disordered carbon assigned to AHSC3 is also observed near  $24^{\circ}$ , confirming the successful composite of lithium hydroxide with the supporting matrix of AHSC3.

To identify the nature of the pore structure of the carbonaceous supporting matrix, nitrogen adsorption–desorption isotherms were performed. Fig. 4(d) presents that compared with the hollow COF (Fig. S7), the surge of CHSC(800) in the low relative pressure region and the absence of an obvious hysteresis loop reveal its identity as a microporous material, and its corresponding surface area ( $871.2$   $\text{m}^2$   $\text{g}^{-1}$ ) not only exhibits a substantial increase over COF ( $38.3$   $\text{m}^2$   $\text{g}^{-1}$ ) but also is superior to other CHSCs [44]. In order not to bury the infinite potential of the precious spherical carbon with internal vacuum caverns of CHSC(800), chemical activation of CHSC(800)/KOH with different mass ratios was applied to

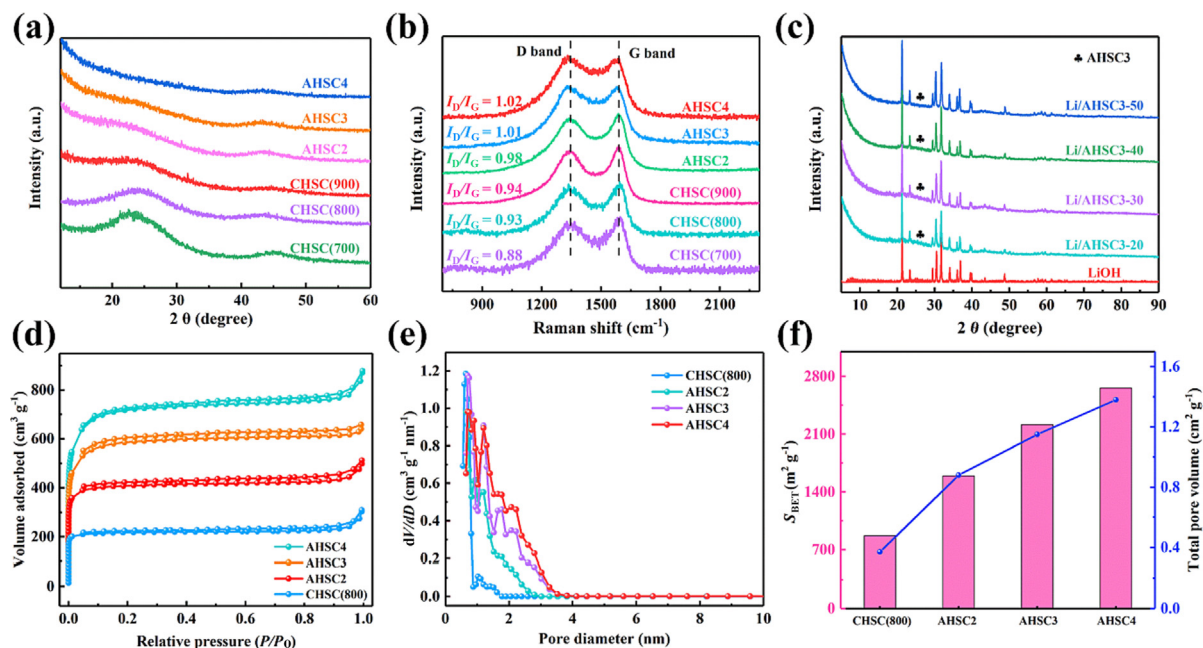


**Fig. 4.** (a) XRD patterns. (b) Raman spectra of CHSCs as well as AHSCs. (c) XRD patterns of LiOH and Li/AHSC3 with various salt ratios. (d)  $N_2$  adsorption/desorption isotherms, (e) pore size distribution, (f)  $S_{BET}$  and pore volume of CHSC(800), AHSC2, AHSC3, AHSC4.

improve its surface area as well as pore structure. Indeed, the isotherms of the formed AHSCs continue to proliferate in the low relative pressure region and show a conspicuous hysteresis loop in the relative pressure region, which elucidates the coexistence of micropores and mesopores in AHSCs [45]. On the other hand, the fact that CHSC(800) merely distributes in the microporous region and the ratio of mesopores in AHSC is synchronized with the increase in activation degree also provides solid evidence for the above inference (Fig. 4e). Besides, Fig. 4(f) and Table S1 display that all AHSCs receive a leapfrog enhancement in surface area and pore volume compared to CHSC(800), confirming the enormous contribution of chemical activation in optimizing the pore structure and improving the surface area. It is noteworthy that despite the optimal surface area ( $2660.5 \text{ m}^2 \text{ g}^{-1}$ ) and pore volume ( $1.39 \text{ cm}^3 \text{ g}^{-1}$ ) of AHSC4, the loss of its internal precious cavity framework due to overactivation may not compensate for its insufficient strength as a supporting matrix in enhancing the key properties of the THS material, which highlights the importance of appropriate activation for specific property enhancement of carbonaceous materials with special applications. Consequently, it is reasonable speculation that AHSC3 with a complete hollow framework and diversified porous structures as well as ultra-high surface area ( $2217.1 \text{ m}^2 \text{ g}^{-1}$ ) not only offers an ideal microchannel for the diffusion of vapor but is also beneficial to the good diffusion and the mass transfer of lithium hydroxide, ensuring its outstanding qualification as the supporting matrix of THS materials.

### 3.2. Hydration property

It is widely acknowledged that the hydration properties of hygroscopic salt-based THS materials occupy a very critical position with respect to their corresponding storage strengths based on the fact that water is the key chemical reaction medium for hygroscopic salts heat storage materials. Therefore, in order to tease out the connection between the nanostructure of the supporting matrix and the hydration properties of THS composites and to filter a standout candidate from a series of supporting matrices, the hydration properties of LiOH thermochemical heat storage materials with various supporting matrices were

exhaustively investigated. It can be found from Fig. 5(a) that the hydration properties of each Li/CHSC-20 display a moderate improvement compared to pristine lithium hydroxide, among which Li/CHSC(800)-20 is more prominent. It should also be clearly recognized that CHSC(800) still has much room for improvement as a supporting matrix of THS materials. To further exploit the unlimited advantages of the precious spherical carbon with internal vacuum caverns of CHSC(800), the necessity of further chemical activation was manifested and confirmed by the dramatic enhancement of hydration properties of Li/AHSC-20. Among them, Li/AHSC3-20 has the fastest hydration kinetics rate and its corresponding water sorption value is able to reach up to  $0.48 \text{ g g}^{-1}$ . Furthermore, a striking fact is that the hydration properties of each material are synchronized with changes in the defectivity and surface area of the corresponding supporting matrix according to the Raman as well as BET results, which not only verifies the close link between the nanostructure of the supporting matrix and the hydration properties of the THS material but also further highlights the effectiveness of optimizing the pore structure through chemical activation. On the other hand, in order to delve deeper into the impact of the nanostructure of the supporting matrix on the water sorption properties, detailed studies of the water sorption values of each material under different humidity conditions were also carried out. From Fig. 5(b), it can be observed that rising humidity conditions have a positive effect on the water sorption value of each material. For example, when the relative humidity (RH) varies ( $50\% \rightarrow 80\%$ ), the sorption value of Li/AHSC3-20 also changes accordingly ( $0.35 \rightarrow 0.48 \text{ g g}^{-1}$ ). Besides, the water sorption values of the THS materials with the hollow spherical carbon acquired after chemical activation as the supporting matrix show a non-negligible improvement compared with Li/CHSC(700)-20, Li/CHSC(800)-20, and Li/CHSC(900)-20 under different humidity conditions. The justifiable explanation for the above results is that as the supporting matrix of the Li/AHSC3 composite, AHSC3 undertakes the pivotal responsibility of the loading platform and the sorption medium with the assistance of the valuable properties of the void spherical framework, high surface area and multimodal porosity, and each type of architectural features of AHSC3 shoulders different liabilities in enhancing storage strength. Specifically,

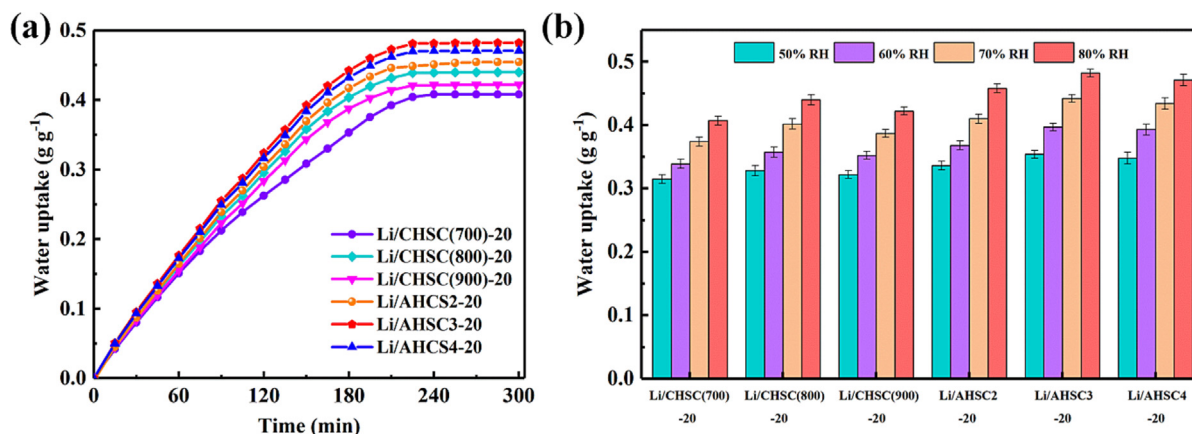


Fig. 5. (a) Water sorption curves of LiOH-THS materials under 30 °C and 80% RH. (b) Water sorption value of LiOH-THS materials at 30 °C with various RH.

the 3D spherical cavity structure with regular geometry and mesopores provides shorter transfer pathways as well as ideal microchannels for adequate diffusion of vapor and salts, which are beneficial for further enhancement of heat and mass transfer performance, while micropores and high surface area jointly promote the contact effect of salt and AHSC3 [46,47]. As a result, benefiting from the combined effect of the above structural advantages, the long-term bottleneck problem of pure LiOH as a hydrated salt is significantly alleviated, and the corresponding hydration properties and storage capacity of Li/AHSC3 composites have also made a remarkable leap forward.

Based on the determination of AHSC3 as the optimal supporting matrix, an investigation of the link between the salt ratio and the hydration properties of LiOH-THS composites was carried out. As depicted in Fig. 6(a), although all materials reach sorption equilibrium at similar times, all Li/AHSC3 composites exhibit tremendously boosted water sorption values compared to LiOH, which also indirectly reflects the obvious improvement of the hydration rate of the composites, and Li/AHSC3-40 demonstrates the best water sorption rate and value of 0.52 g g<sup>-1</sup>. The above results show that under the assistance of the supporting matrix of AHSC3 with the void spherical framework, high surface area as well as multi-modal porosity, not only the uniform dispersion of the salt grains can be achieved, but also the hydration process of the vapor and the salt grains can be promoted, which displayed as a dramatical improvement of the hydration properties of the Li/AHSC3

composite [48]. It is noteworthy that as the salt ratio varies from 20% to 40%, the corresponding kinetics rate and water sorption values of the Li/AHSC3 composites under the same humidity conditions also show a synchronous increasing trend from 0.48 to 0.52 g g<sup>-1</sup>. Surprisingly, when the salt ratio is changed to 50%, the kinetics rate, as well as the sorption value of Li/AHSC3-50, does not continue to increase as expected. The reason responsible for this unusual reversal may be the relatively extravagant salt ratio in Li/AHSC3-50, which not only provokes the defective nature of agglutination in hygroscopic salts and undermines the role of the supporting matrix of AHSC3 in improving the salt dispersibility, but also hampers the hydration process of the salt and vapor, and eventually incubates irreversible decay of the hydration properties of the THS materials [49]. The SEM image of Li/AHSC3-50 (Fig. S3) also supports this conjecture. On the other hand, the water sorption value of Li/AHSC3 with different LiOH ratios and pristine salt under various humidity conditions was also studied. As shown in Fig. 6(b), when each Li/AHSC3 is exposed to lower humidity conditions, their respective water sorption differences and trends are indistinguishable from those observed at 80% RH, which further proves the wide applicability of the above conclusions under different humidity conditions. Moreover, the water sorption of all Li/AHSC3s exhibit different degrees of improvement compared with lithium hydroxide, and the changing trend is synchronized with the humidity conditions. Obviously, the above findings not only reveal the delicate balance between hygroscopic salts and

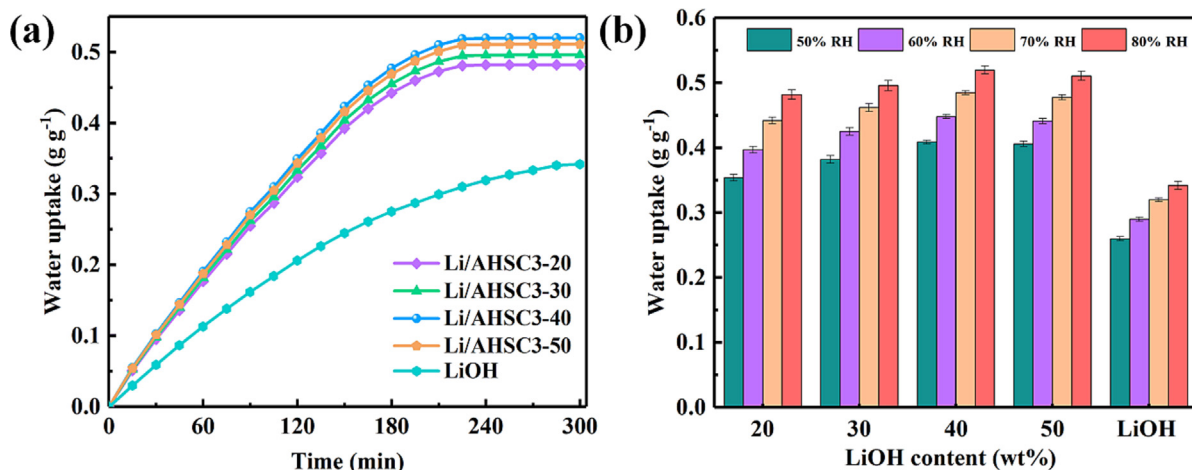


Fig. 6. (a) Water sorption curves of pristine salt and Li/AHSC3-x under 30 °C and 80% RH. (b) Water sorption value of pristine salt and Li/AHSC3-x under 30 °C with different RH.



supporting matrix in Li/AHSC3, but also further highlight the key significance of AHSC3 as a supporting matrix for the improvement of hydration properties of LiOH·THS composites.

In order to shed more light on the specific effects of humidity conditions and operating temperature on the hydration properties of THS materials, the hydration properties of Li/AHSC3-40 under various humidity conditions and operating temperatures were explored. Fig. 7(a) displays that when the humidity condition becomes the only variable (50% → 80%), the water sorption value of the Li/AHSC3-40 under different humidity is synchronized with the trend of RH, but it has almost no effect on the respective time span of reaching the sorption steady state, which demonstrates that the increase in humidity indirectly promotes the increase of the hydration kinetics rate while enhancing the water sorption value. It can be found from Fig. 7(b) that when the operating temperature is the only variable (25 → 45 °C), the time span for the Li/AHSC3-40 to complete the sorption steady at different temperatures shortens significantly with the increase of temperature while the respective water sorption value hardly fluctuates, indicating that higher temperature contributes to the improvement of moisture content, and finally achieves the improvement of adsorption rate. In addition, it is commendable that Li/AHSC3-40 showed no signs of coacervation and deliquescence throughout the testing process, further highlighting the positive and critical role of AHSC3 as a loading platform and the sorption medium for LiOH·THS composites in assisting hygroscopic salts to overcome their defective and disadvantageous nature. Based on the results of the entire hydration property exploration campaign, it is a logical inference for the superb storage strength of the Li/AHSC3 composites.

### 3.3. Thermochemical heat storage

In order to gain a deep insight into the structure–property connection between supporting matrix and storage strength on the basis of the exploration of hydration properties, the storage strength of a series of LiOH·THS composites with various supporting matrices was comprehensively investigated. As depicted in Fig. 8(a–c), each Li/CHSC-20 exhibits a decently improved storage strength over LiOH with Li/CHSC(800)-20 showing the greatest improvement of 1053.7 kJ kg<sup>−1</sup> by virtue of the spherical hollow structure of CHSC that provides shorter transfer pathways and abundant channels for adequate diffusion of vapor and salts. Nonetheless, it cannot be ignored that only shortening the diffusion channel has a limited impact on the advancement of the storage strength of the THS material. Consequently, under the premise of maintaining the advantages of the void spherical framework,

further regulating the pore structure of the supporting matrix and improving its surface area have become the primary tasks to maximize the storage strength of the LiOH·THS material. As a proof-of-concept, Fig. 8(d and e) and Fig. 9(b) present an astonishing improvement in storage strength for all Li/AHSC-20 composites using AHSC that unify the superiorities of the void spherical framework, high surface area as well as multimodal porosity as supporting matrices and Li/AHSC3-20 displays the most prominent storage density of 1429.7 kJ kg<sup>−1</sup>, further highlighting the necessity of the chemical activation strategy and the structural superiority of AHSC. In addition, it is crystal clear from Fig. 8(f) that the storage strength of the LiOH·THS material has a trend of changing in synchronization with the hydration properties, which unambiguously indicates the fact that the nanostructure of the supporting matrix, hydration properties, and storage strength of the composites are inseparable. On the other hand, it also serves as further evidence for the key contribution of AHSC3 as a supporting matrix to the improvement of the storage strength of the THS composites.

Under the premise of selecting AHSC3 as the optimal supporting matrix, a study was launched on the connection between the salt ratio and the storage strength of Li/AHSC3 materials. It can be observed from Fig. 9(a) that the storage strength of LiOH is merely 502.3 kJ kg<sup>−1</sup>, originating from the poor hydration ability of pristine lithium hydroxide owing to the serious coacervation of pristine salt with a bulky size. As a result, this inherent limitation prevents LiOH from fulfilling its potential for heat storage. On the other hand, Fig. 9(b–e) display that the storage strengths of each Li/AHSC3 material exhibit a leapfrog growth over LiOH, and Li/AHSC3-40 (1916.4 kJ kg<sup>−1</sup>) is nearly 3.81 times higher than that of LiOH. The source of this occurrence is that with the synergistic help of a 3D spherical cavity framework, high surface area as well as multimodal porosity, AHSC3 outstandingly undertakes the liability of providing a loading platform and the sorption medium for hygroscopic salts, which not only has a positive effect on enhancing the dispersibility of hygroscopic salts and the adsorption/diffusion of vapors across the composites, but also lubricates the contact between the salt, supporting matrix, and moisture, thus achieving the goal of enhancing the storage strength of the LiOH·THS material [50]. Noticeably, Fig. 9(f) displays that as the salt ratio varies from 20% to 40%, the corresponding storage strength of Li/AHSC3 also demonstrates a synchronous upward tendency from 1429.7 to 1916.4 kJ kg<sup>−1</sup>. Unexpectedly, when the salt ratio is changed to 50%, the storage strength of Li/AHSC3-50 does not follow the previous upward trend but decreases to 1842.3 kJ kg<sup>−1</sup>. The culprit for the trend break might be the relatively high salt ratio of Li/AHSC3-50, which disturbs the hydration

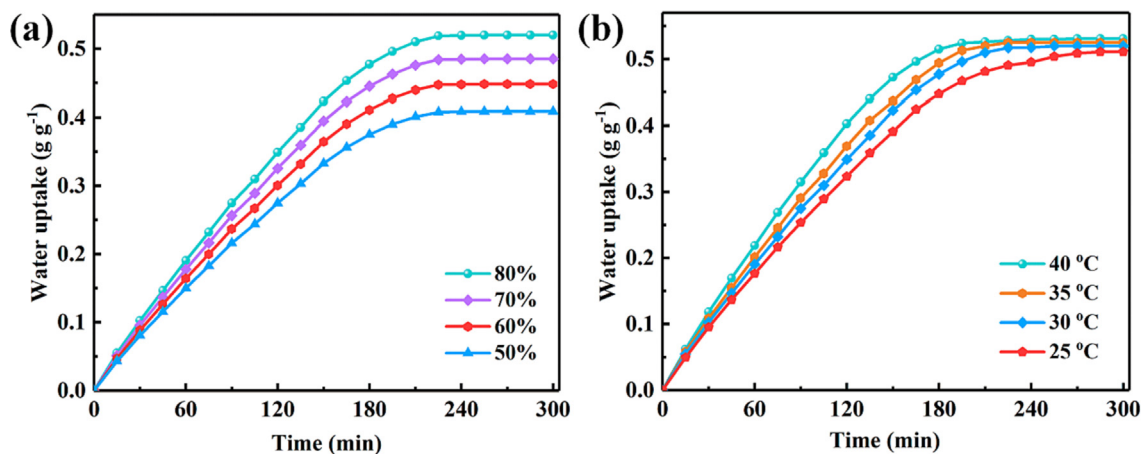
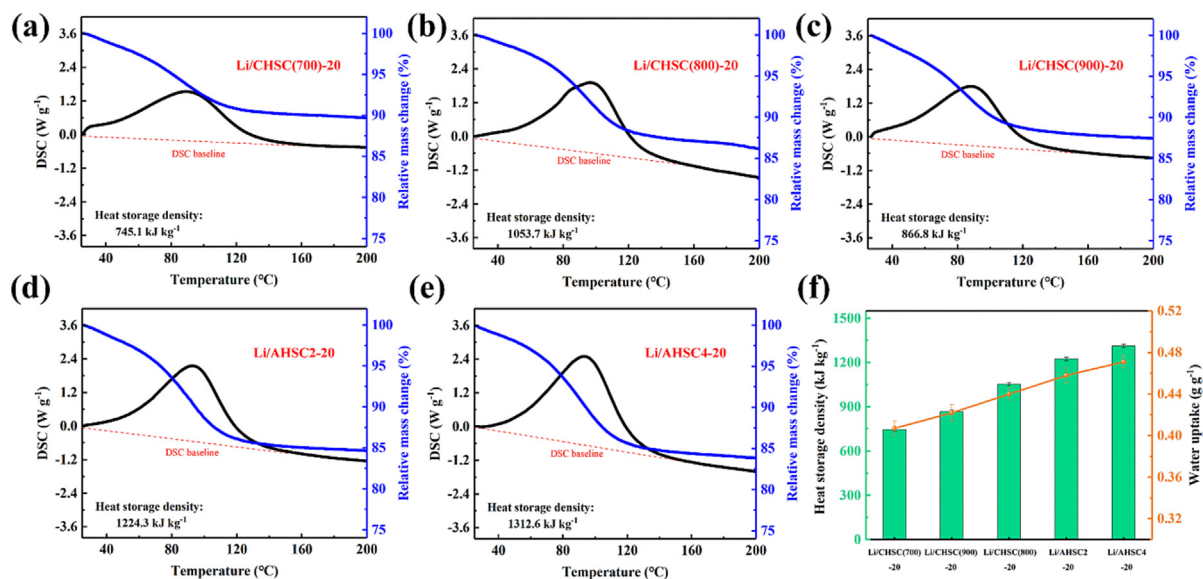
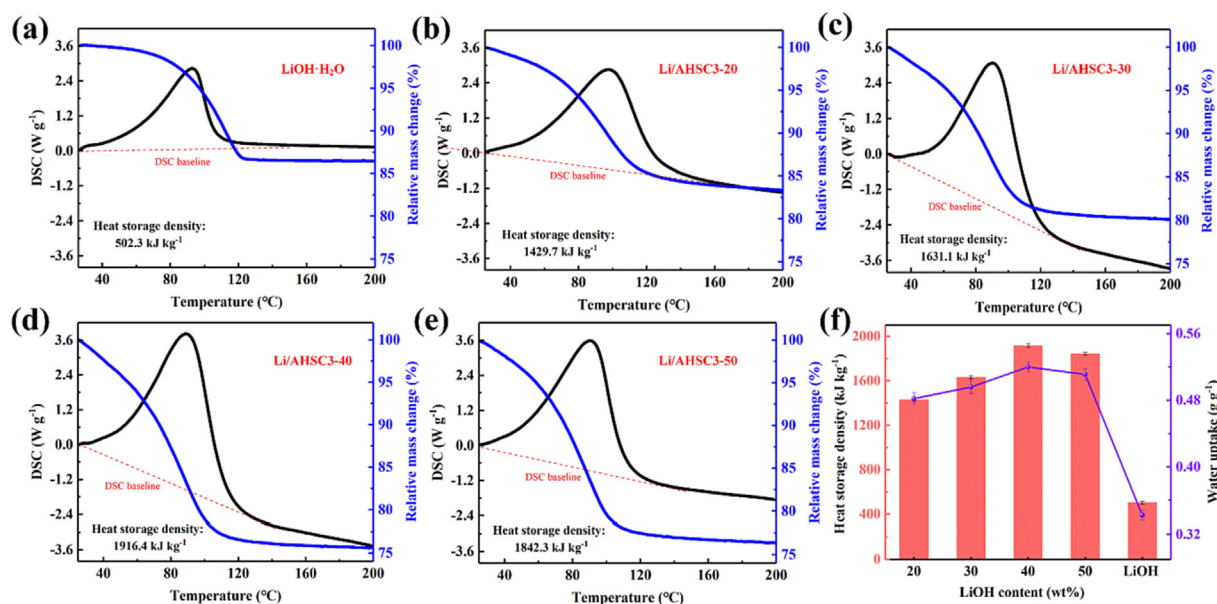


Fig. 7. (a) Water sorption curves of Li/AHSC3-40 at 30 °C with various RH. (b) Water sorption curves of Li/AHSC3-40 at 80% RH with various operating temperatures.



**Fig. 8.** STA images of (a) Li/CHSC(700)-20, (b) Li/CHSC(800)-20, (c) Li/CHSC(900)-20, (d) Li/AHSC2-20, (e) Li/AHSC4-20. (f) The changing trend around storage strength as well as sorption value of various THS materials.



**Fig. 9.** STA images of (a) LiOH, (b–e) Li/AHSC3-20, Li/AHSC3-30, Li/AHSC3-40, Li/AHSC3-50. (f) The changing trend of storage strength and sorption value with the ratio of salt in Li/AHSC3.

between the hygroscopic salt and vapor while worsening the self-aggregation of the hygroscopic salt, causing a decline in the hydration properties and storage strength of the THS materials [51]. Besides, the storage strength of Li/AHSC3 shows a step-by-step trend with the change of hydration properties, further elucidating the close correlation between hydration properties and storage strength of LiOH-THS materials. Supported by the above results, it is optimistic to predict that Li/AHSC3-40 with outstanding hydration properties and storage strength may trigger a new revolution in the durable storage of low-grade heat.

### 3.4. Cyclability and thermal conductivity

It is a well-known fact that the cyclability of THS materials has great reference value for its future engineering applications. In this

regard, the cyclability of Li/AHSC3-40 and LiOH through successive adsorption–desorption was studied and the relative mass change was introduced to reflect the fluctuation of water adsorption during the cycle. As depicted in Fig. 10(a), the storage strength and water sorption of LiOH are significantly degraded by 72.2% and 75.8% with the concomitant severe coaggregation and deliquescence after twenty-five cycles, which is a relatively serious degree of attenuation and exposes the insurmountable defects of the hygroscopic salt itself. In comparison, Fig. 10(d) demonstrates that the storage strength and water sorption of Li/AHSC3-40 just display a tiny degeneration of 5.5% and 5.9%, and the morphology (Fig. S8) and pore structure (Table S1) are almost identical to those before cycling, highlighting the vital duty of AHSC3 as a supporting matrix in ameliorating cycle stability. The explanation for this fact is that the degree of aggregation of pure LiOH after the cycle was much



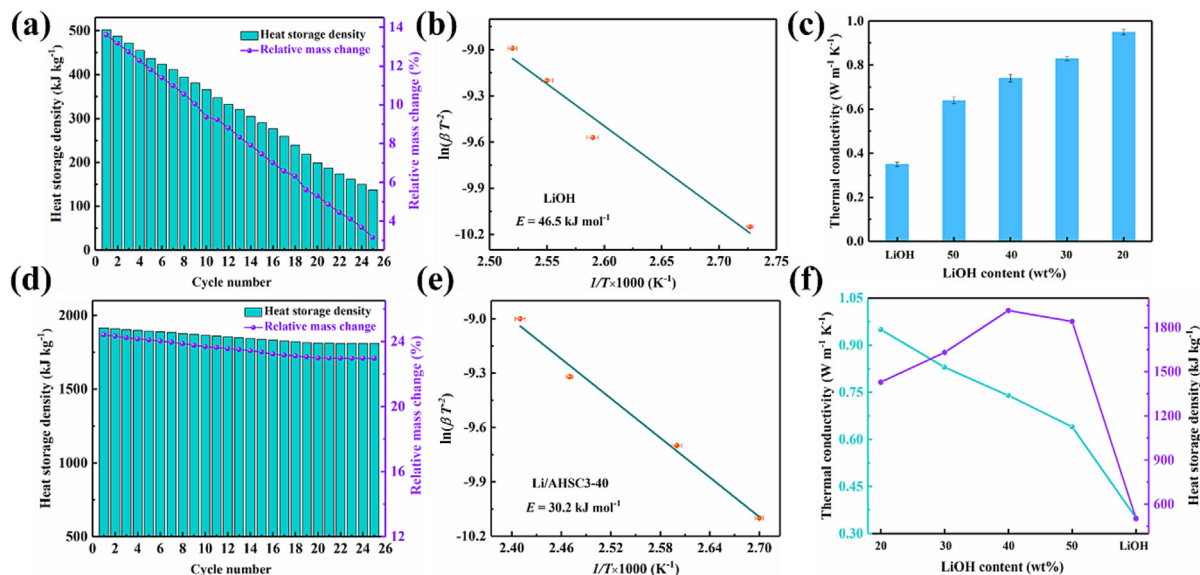


**Fig. 10.** Cyclability and the activation energy of (a and b) lithium hydroxide, (d and e) Li/AHSC3-40. (c) Thermal conductivity, (f) the trend of thermal conductivity with storage strength of lithium hydroxide and Li/AHSC3-20, Li/AHSC3-30, Li/AHSC3-40, Li/AHSC3-50.

higher than that of LiOH in Li/AHSC3-40 and the liquid leakage and encrustation of pure LiOH were also clearly observed, which hinders the full hydration of pure LiOH with vapor, thereby making the decay degree of pure LiOH more serious after cycling [52]. Noticeably, Fig. 10(b and e) display that there is a conspicuous activation energy gap between lithium hydroxide ( $46.5 \text{ kJ mol}^{-1}$ ) and Li/AHSC3-40 ( $30.2 \text{ kJ mol}^{-1}$ ), which not only indicates that Li/AHSC3-40 has a relatively smooth hydration process but also makes the outstanding cyclability of Li/AHSC3-40 a more tenable fact.

It is a widely recognized fact that thermal conductivity is an important indicator affecting the heat exchange efficiency within the reaction bed, and a decent thermal conductivity will greatly improve the feasibility of THS materials in engineering implementation and commercialization. Fig. 10(c) displays that all Li/AHSC3 composites present a conspicuously enhanced thermal conductivity over lithium hydroxide ( $0.35 \text{ W m}^{-1} \text{ K}^{-1}$ ) with the help of the great thermal conductivity of AHSC3, which demonstrates the value of the supporting matrix in endowing the THS composites with higher heat transfer potential and Li/AHSC3-20 ( $0.95 \text{ W m}^{-1} \text{ K}^{-1}$ ) exhibits the most obvious thermal

conductivity improvement. It is noteworthy from Fig. 10(f) that when faced with a dilemma between thermal conductivity and storage strength, Li/AHSC3-40 with the best storage strength and good thermal conductivity ( $0.74 \text{ W m}^{-1} \text{ K}^{-1}$ ) has become the optimal alternative based on comprehensive consideration of heat transfer properties and storage strength. On the other hand, Table 1 presents that the heat storage parameters of Li/AHSC3-40 are more eye-catching compared to other THS materials. It is noteworthy that the cost of Li/AHSC3-40 is around  $\$55.2 \text{ kg}^{-1}$  calculated by the cost of 1,3,5-tris(4-aminophenyl)-benzene ( $\$203.7 \text{ kg}^{-1}$ ), 4-formylphenylboronic acid ( $\$148.2 \text{ kg}^{-1}$ ), potassium hydroxide ( $\$4.1 \text{ kg}^{-1}$ ), and lithium hydroxide ( $\$19.7 \text{ kg}^{-1}$ ), which is expensive than commonly used THS materials and also reflects the need for further cost reduction for its future practical implementation [27,28]. Hence, it is a valid assumption according to the above results that Li/AHSC3-40, which not only possesses superb storage strength and hydration properties but also exhibits impressive cyclability and thermal conductivity, will become a well-known representative of THS materials in the field of low-grade heat storage as well as engineering applications.

**Table 1**  
Comparison of Li/AHSC3-40 composite and other THS composites.

THS composite	Charging temperature (°C)	Equilibrium absorption ( $\text{g g}^{-1}$ )	Energy density ( $\text{kJ kg}^{-1}$ )	Thermal conductivity ( $\text{W m}^{-1} \text{ K}^{-1}$ )	Ref.
SrBr <sub>2</sub> /natural graphite	150	0.42	600	2.3	[53]
LiCl-LiOH/expanded graphite	85	0.7	1400	1.2	[35]
CaCl <sub>2</sub> /silica-alumina	200	0.4	700	\	[54]
MIL-101(Cr)	40	0.95	1950	\	[55]
LiCl/silica gel	90	\	450	\	[56]
MgSO <sub>4</sub> -ZnSO <sub>4</sub>	120	0.23	1422	\	[57]
MIL-101(Cr)/carbon foam	47	1.2	2541.6	\	[58]
ZnSO <sub>4</sub> /zeolite	200	0.25	934	\	[59]
SrCl <sub>2</sub> /MgSO <sub>4</sub>	150	0.48	960	\	[60]
CaCl <sub>2</sub> /MIL-101(Cr)	200	0.60	1274	\	[61]
LiCl/activated alumina	120	0.41	1041	\	[62]
LiCl/hollow SiO <sub>2</sub>	100	0.22	750	\	[63]
SrBr <sub>2</sub> /MIL-101(Cr)	80	0.28	1350	\	[64]
LiCl@UiO-66	90	0.27	900	\	[65]
Li/AHSC3-40	120	0.52	1916.4	0.95	This work

## 4. Conclusions

In summary, we have proved that AHSC3 excellently fulfills its role as a supporting matrix and the synthesized Li/AHSC3-40 has also been displayed to be a great hygroscopic salt THS material. Based on the continuation of the unique hollow structures with the 3D spherical shape of CHSC(800), AHSC3 has further improved the surface area and diversified the pore architecture via KOH activation, which allows it to unify the superiorities of the void spherical framework, high surface area, and multimodal porosity while compensating the shortcomings of their respective structures. As the supporting matrix of the Li/AHSC3 composite, AHSC3 shoulders the important responsibility of the loading platform and the sorption medium with the assistance of these valuable properties, which not only helps to improve the salt dispersibility and water adsorption/diffusion in the LiOH-THS composite but also enhances the actual hydration properties and storage strength. In fact, the fabricated Li/AHSC3 exhibits fabulous storage strength (max. 1916.4 kJ kg<sup>-1</sup>) and water sorption performance. In addition, Li/AHSC3-40 with enhanced thermal conductivity displays a low strength drop of 5.5% after twenty-five reciprocating cycles, elucidating its excellent cyclability and heat transfer capability. This study not only builds a traversable bridge for efficient harvesting of low-grade heat energy but also may shed a novel insight into the design of well-defined spherical porous carbonaceous material with a hollow structure based on COFs for a wide variety of applications.

## Declaration of competing interest

The authors declare that they have no known competing financial interests or personal relationships that could have appeared to influence the work reported in this paper.

## Acknowledgments

The authors appreciate the support from the Key-Area Research and Development Program of Guangdong Province (2020B0202010004), the National Natural Science Foundation of China (52071192), and the Key Research Program of Frontier Sciences, CAS (QYZDY-SSW-JSC038).

## Appendix A. Supplementary data

Supplementary data to this article can be found online at <https://doi.org/10.1016/j.jechem.2022.06.022>.

## References

- [1] X. Zhao, Z. Zhang, J. Chen, G. Liao, F. Zhang, E. Leng, D. Han, W. Hu, *Appl. Energy* 257 (2020) 113995.
- [2] R. Wu, W. Gao, Y. Zhou, Z. Wang, Q. Lin, *Compos. Part B: Eng.* 225 (2021) 109318.
- [3] X. Geng, Y. Gao, N. Wang, N. Han, X. Zhang, W. Li, *Chem. Eng. J.* 408 (2021) 127276.
- [4] G. Alva, Y. Lin, G. Fang, *Energy* 144 (2018) 341–378.
- [5] S. Koohi-Fayegh, M.A. Rosen, *J. Energy Storage* 27 (2020) 101047.
- [6] Z. Niu, S. Qi, S.S.A. Shuaib, W. Yuan, *Compos. Part B: Eng.* 228 (2022) 109431.
- [7] H. Peng, J. Raya, F. Richard, W. Baaziz, O. Ersen, A. Ciesielski, P. Samorì, *Angew. Chem. Int. Ed.* 59 (2020) 19602–19609.
- [8] F. Kuznik, K. Johannes, C. Obrecht, D. David, *Renew. Sustain. Energy Rev.* 94 (2018) 576–586.
- [9] M. Biesuz, F. Valentini, M. Bortolotti, A. Zambotti, F. Cestari, A. Bruni, V.M. Sglavo, G.D. Sorarù, A. Dorigato, A. Pegoretti, *Renew. Energy* 178 (2021) 96–107.
- [10] H. Yang, Y. Liu, J. Li, C. Wang, Y. Li, *Chem. Eng. J.* 403 (2021) 126406.
- [11] J. Guo, D. Jiang, *ACS Cent. Sci.* 6 (2020) 869–879.
- [12] X. Guan, F. Chen, Q. Fang, S. Qiu, *Chem. Soc. Rev.* 49 (2020) 1357–1384.
- [13] I. Ahmed, S.H. Jhung, *Coord. Chem. Rev.* 441 (2021) 213989.
- [14] K. Geng, T. He, R. Liu, S. Dalapati, K.T. Tan, Z. Li, S. Tao, Y. Gong, Q. Jiang, D. Jiang, *Chem. Rev.* 120 (2020) 8814–8933.
- [15] Q. Guan, L.-L. Zhou, L.-N. Zhou, M. Li, G.-X. Qin, W.-Y. Li, Y.-A. Li, Y.-B. Dong, *Chem. Commun.* 56 (2020) 7793–7796.
- [16] L. Wang, Y. Yang, H. Liang, N. Wu, X. Peng, L. Wang, Y. Song, *J. Hazard. Mater.* 409 (2021) 124528.
- [17] S. Zhang, W. Xia, Q. Yang, Y. Valentino Kaneti, X. Xu, S.M. Alshehri, T. Ahamed, M.S.A. Hossain, J. Na, J. Tang, Y. Yamauchi, *Chem. Eng. J.* 396 (2020) 125154.
- [18] W. Yang, J. Li, L. Lan, Y. Zhang, H. Liu, *Chem. Eng. J.* 390 (2020) 124581.
- [19] T. Jiang, W. Jiang, Y. Li, Y. Xu, M. Zhao, *Carbon* 180 (2021) 92–100.
- [20] L. Li, L. Li, C. Cui, H. Fan, R. Wang, *ChemSusChem* 10 (2017) 4921–4926.
- [21] M. Kim, T. Park, C. Wang, J. Tang, H. Lim, M.S.A. Hossain, M. Konarova, J.W. Yi, J. Na, J. Kim, Y. Yamauchi, *ACS Appl. Mater. Interfaces* 12 (2020) 34065–34073.
- [22] L.F. Cabeza, A. de Gracia, G. Zsembinszki, E. Borri, *Energy* 231 (2021) 120943.
- [23] X. Sheng, D. Dong, X. Lu, L. Zhang, Y. Chen, *Compos. A Appl. Sci. Manuf.* 138 (2020) 106067.
- [24] Y. Zhang, R. Wang, *Energy Stor. Mater.* 27 (2020) 352–369.
- [25] P. Pardo, A. Deydier, Z. Anxionnaz-Minvielle, S. Rougé, M. Cabassud, P. Cognet, *Renew. Sustain. Energy Rev.* 32 (2014) 591–610.
- [26] Y. Li, N. Kumar, J. Hirsche, D.O. Akamo, K. Li, T. Tugba, M. Goswami, R. Orlando, T.J. LaClair, S. Graham, K.R. Gluesenkamp, *Compos. Part B: Eng.* 233 (2022) 109621.
- [27] J. Zhu, C. Gao, F. Kong, K. Zhang, Z. Bai, J. Guo, *Sol. Energy Mater. Sol. Cell* 229 (2021) 111118.
- [28] J. Lin, Q. Zhao, H. Huang, H. Mao, Y. Liu, Y. Xiao, *Sol. Energy* 214 (2021) 149–178.
- [29] H. Liu, W. Wang, Y. Zhang, *J. Clean. Prod.* 313 (2021) 127908.
- [30] B.C. Zhao, T.X. Li, J.C. Gao, R.Z. Wang, *Renew. Sustain. Energy Rev.* 121 (2020) 109712.
- [31] Q. Zhao, J. Lin, H. Huang, Q. Wu, Y. Shen, Y. Xiao, *Energy Build.* 244 (2021) 111035.
- [32] A. Solé, I. Martorell, L.F. Cabeza, *Renew. Sustain. Energy Rev.* 47 (2015) 386–398.
- [33] S. Li, H. Huang, X. Yang, Y. Bai, J. Li, N. Kobayashi, M. Kubota, *Appl. Therm. Eng.* 128 (2018) 706–711.
- [34] W. Li, J.J. Klemeš, Q. Wang, M. Zeng, *Renew. Energy* 157 (2020) 920–940.
- [35] W. Li, J.J. Klemeš, Q. Wang, M. Zeng, *Chem. Eng. J.* 421 (2021) 129586.
- [36] W. Li, J.J. Klemeš, Q. Wang, M. Zeng, *J. Clean. Prod.* 285 (2021) 124907.
- [37] S. Kandambeth, V. Venkatesh, D.B. Shinde, S. Kumari, A. Halder, S. Verma, R. Banerjee, *Nat. Commun.* 6 (2015) 6786.
- [38] W. Weng, J. Lin, Y. Du, X. Ge, X. Zhou, J. Bao, *J. Mater. Chem. A* 6 (2018) 10168–10175.
- [39] R. Wang, D. Jin, Y. Zhang, S. Wang, J. Lang, X. Yan, L. Zhang, *J. Mater. Chem. A* 5 (2017) 292–302.
- [40] X. Chen, Y. Xu, F.-H. Du, Y. Wang, *Small Methods* 3 (2019) 1900338.
- [41] Y. Zeng, R. Zou, Z. Luo, H. Zhang, X. Yao, X. Ma, R. Zou, Y. Zhao, *J. Am. Chem. Soc.* 137 (2015) 1020–1023.
- [42] F. Bai, Y. Xia, B. Chen, H. Su, Y. Zhu, *Carbon* 79 (2014) 213–226.
- [43] S. Yang, X. Li, T. Tan, J. Mao, Q. Xu, M. Liu, Q. Miao, B. Mei, P. Qiao, S. Gu, F. Sun, J. Ma, G. Zeng, Z. Jiang, *Appl. Catal. B: Environ.* 307 (2022) 121147.
- [44] Q. Xu, H. Zhang, Y. Guo, J. Qian, S. Yang, D. Luo, P. Gao, D. Wu, X. Li, Z. Jiang, *Y. Sun, Small* 15 (2019) 1905363.
- [45] X. Hu, Y. Long, M. Fan, M. Yuan, H. Zhao, J. Ma, Z. Dong, *Appl. Catal. B: Environ.* 244 (2019) 25–35.
- [46] L. Garzón-Tovar, J. Pérez-Carvajal, I. Imaz, D. Maspoch, *Adv. Funct. Mater.* 27 (2017) 1606424.
- [47] Y. Qin, X. Han, Y. Li, A. Han, W. Liu, H. Xu, J. Liu, *ACS Catal.* 10 (2020) 5973–5978.
- [48] S. Li, H. Huang, J. Li, N. Kobayashi, Y. Osaka, Z. He, H. Yuan, *RSC Adv.* 8 (2018) 8199–8208.
- [49] Q. Wang, Y. Xie, B. Ding, G. Yu, F. Ye, C. Xu, *Sol Energy Mater Sol Cell.* 200 (2019) 110047.
- [50] C. Xu, Z. Yu, Y. Xie, Y. Ren, F. Ye, X. Ju, *Appl. Therm. Eng.* 129 (2018) 250–259.
- [51] T. Yan, T. Li, J. Xu, J. Chao, R. Wang, Y.I. Aristov, L.G. Gordeeva, P. Dutta, S.S. Murthy, *ACS Energy Lett.* 6 (2021) 1795–1802.
- [52] M. Kubota, S. Matsumoto, H. Matsuda, *Appl. Therm. Eng.* 150 (2019) 858–863.
- [53] A. Cammarata, V. Verda, A. Sciacovelli, Y. Ding, *Energy Convers. Manage.* 166 (2018) 233–240.
- [54] A. Jabbari-Hichri, S. Bennici, A. Auroux, *Sol. Energy Mater. Sol. Cell* 140 (2015) 351–360.
- [55] C. Wang, L. Hua, H. Yan, B. Li, Y. Tu, R. Wang, *Joule* 4 (2020) 435–447.
- [56] V. Palomba, A. Sapienza, Y. Aristov, *Appl. Energy* 248 (2019) 299–309.
- [57] A.U. Rehman, M. Khan, Z. Maosheng, *J. Energy Stor.* 26 (2019) 101026.
- [58] J. Xu, J. Chao, T. Li, T. Yan, S. Wu, M. Wu, B. Zhao, R. Wang, *ACS Cent. Sci.* 6 (2020) 1542–1554.
- [59] A. Ur Rehman, Z. Maosheng, A. Hayat, *Int. J. Energy Res.* 44 (2020) 269–281.
- [60] W. Li, M. Zeng, Q. Wang, *Sol. Energy Mater. Sol. Cell.* 210 (2020) 110509.
- [61] W. Shi, Y. Zhu, C. Shen, J. Shi, G. Xu, X. Xiao, R. Cao, *Microporous Mesoporous Mater.* 285 (2019) 129–136.
- [62] Y.N. Zhang, R.Z. Wang, T.X. Li, *Energy* 156 (2018) 240–249.
- [63] A. Shkatulov, R. Joosten, H. Fischer, H. Huinink, *ACS Appl. Energy Mater.* 3 (2020) 6860–6869.
- [64] P. D'Ans, E. Courbon, A. Permyakova, F. Nouar, C. Simonnet-Jégat, F. Bourdreux, L. Malet, C. Serre, M. Frère, N. Steunou, *J. Energy Stor.* 25 (2019) 100881.
- [65] Y. Sun, A. Spieß, C. Jansen, A. Nuhnen, S. Gökpinar, R. Wiedey, S.-J. Ernst, C. Janiak, *J. Mater. Chem. A* 8 (2020) 13364–13375.